

---

# MODELLING INTERSTELLAR EXTINCTION IN STELLAR POPULATIONS

---

M.Phil. thesis

**Alexander Lisboa-Wright**

---

Astrophysics Research Institute, Liverpool John Moores University  
September 2019

## **Abstract**

## Units & Terminology

Unless stated otherwise, all quantities will be described in CGS units (masses in grams, lengths in centimetres, times in seconds, energies in ergs).

In this project, the notation  $\log(x)$  represents the logarithm of  $x$  to the base 10. The natural logarithm of  $x$  will be expressed as  $\ln(x)$ .

$$\begin{aligned}
 M &: \text{mass} \\
 M_{\odot} &= 1.989 \times 10^{33} \text{ g} : \text{solar mass} \\
 L &: \text{luminosity} \\
 L_{\odot} &= 3.842 \times 10^{33} \text{ erg s}^{-1} : \text{solar luminosity} \\
 g &: \text{gravity} \\
 R &: \text{radius} \\
 G &= 6.6723 \times 10^{-8} \text{ cm}^3 \text{ g}^{-1} \text{ s}^{-2} : \text{gravitational constant} \\
 \sigma_{\text{SB}} &= 5.678 \times 10^{-5} \text{ erg cm}^{-2} \text{ K}^{-4} \text{ s}^{-1} : \text{Stefan-Boltzmann constant}
 \end{aligned}$$

# Chapter 1

## Introduction

### 1.1 Extinction definition

As the light emitted from a star travels towards a distant observer, its intensity, or flux,  $f$  decreases with distance  $d$  via an inverse-square law:

$$f = \frac{L}{4\pi d^2} \quad (1.1)$$

where  $L$  is the star's luminosity, which is an intrinsic property of the star (i.e., independent of the observer). Equation 1.1 is a natural consequence of the same light wave expanding outwards from its source into a progressively larger spherical volume of empty space.

However, the interstellar medium is not a perfect vacuum. It contains many different structures, such as diffuse gas clouds, that can absorb or scatter light passing through, depending on the wavelength of the incoming photons, the spacing between the individual atoms (i.e., the density of the medium) and the quantum levels in the atoms occupied by their electrons. These absorption and scattering events are known as interstellar extinction. For a given source, its interstellar extinction coefficient represents the sum of the effects of all extinction events along the line-of-sight between the source and the observer.

Interstellar extinction preferentially affects light at shorter (i.e., bluer) wavelengths. Therefore, the effect of extinction is sometimes referred to as “reddening”, despite the fact that this term is also applied to a related, but distinct, quantity (see Section 1.6). Therefore, it should be expected that sources with proportionally higher fluxes at shorter wavelengths are most affected by extinction.

Extinction is defined using the standard astronomical system of flux magnitudes. In general, the difference between two flux measurements,  $f_1$  and  $f_2$ , in magnitudes, is expressed as:

$$m_1 - m_2 = -2.5 \log \left( \frac{f_1}{f_2} \right) \quad (1.2)$$

where  $m_1$  and  $m_2$  are the magnitudes for  $f_1$  and  $f_2$ , respectively. However, the flux of a source varies intrinsically with the distance travelled by the light to the observer (see Equation 1.1). To account for this, the distances to sufficiently close sources can be determined independently of their flux by measuring the sources' parallax from Earth.

The parallax  $p$  of an object is defined as the angular distance the object moves relative to the “fixed” background stars as the Earth moves a distance of 1AU (the average separation of the Sun and Earth during one complete orbit) perpendicular to the line-of-sight. This allows the distance,  $d$ , to be calculated using the geometry of triangles, combined with the small-angle approximation, as:

$$d/\text{pc} = \frac{1}{(p/\text{arcsec})} \quad (1.3)$$

For more distant stellar sources with much smaller parallaxes, a potential alternative is to view the object in a very long-wavelength filter, in which observations are likely to be impacted much less significantly by extinction, to estimate the type of star being observed, before using theoretical models to compare with observations at different wavelengths. This is more effective for brighter stars.

The role of distance gives each astronomical object two principal flux parameters. These are the apparent magnitude,  $m$ , and the absolute magnitude,  $M$ . The apparent magnitude is the flux magnitude of a source as observed by the telescope. The absolute magnitude is the predicted flux magnitude of the same source if it were to be placed at a fixed distance of 10 parsecs (pc) from the telescope with zero extinction. The absolute magnitude exists for the purpose of stellar classification, as the corresponding flux is simply a constant multiplied by the stellar luminosity (see Equation 1.1), which is an intrinsic physical property of the star.

However, to calculate the absolute magnitude of a source, we first require its distance and extinction coefficient,  $A$ . To account for extinction, it is necessary to define a new quantity, known as the intrinsic apparent magnitude,  $m_0$ . This is defined as the flux magnitude of a source corrected for losses due to extinction but not due to distance. In practice, it represents the apparent magnitude for light passing through a fully-transparent medium. The relation between  $m_0$  and  $M$ , can be found by combining Equations 1.1 and 1.2:

$$m_0 - M = -2.5 \log \left( \left( \frac{10\text{pc}}{d} \right)^2 \right) = 5 \log \left( \frac{d}{\text{pc}} \right) - 5 \quad (1.4)$$

This quantity is known as the distance modulus. As seen in Equation 1.4, it varies only with distance. The quantity  $m - M$ , linking the initial observed data with the

final theoretical data, is known as the apparent distance modulus and varies with both distance and extinction.

Therefore, the extinction coefficient  $A$ , defined as the flux lost due to the effects of the intervening line-of-sight medium, can be defined as:

$$A = m - m_0 \quad (1.5)$$

This fits with the physical definition of interstellar extinction given earlier, i.e. as the flux lost solely due to scattering and absorption in the interstellar medium.

## 1.2 Observational constraints

No telescope can view the sky at all spectral wavelengths - it would be wholly impractical due to the sheer number of sources across the spectrum, as well as the fact that telescope resolution depends on the wavelength of the incoming light. Therefore, modern telescopes are equipped with a system of filters or bands, which allow only light within a narrow range of wavelengths. In a filter system, the individual filters are designed to operate best at different wavelengths. The filter system therefore covers a much wider range of spectral wavelengths than a single filter would alone. This property is used to observe stars at different wavelengths to determine their spectral colour, which in turn grants further physical information about the star (see Section 1.6 for details).

Furthermore, the filters in a given system are designed such that the range of wavelengths in which each can detect incoming light overlaps with those of its neighbour(s), as shown in Figures 2.2-2.3. This ensures that there are no wavelength gaps in which incoming light cannot be detected. This is particularly important for quantum line emission, which occurs only at specific wavelengths for particular electron occupancy levels (see Section 1.5 for exceptions relevant to this project). One of the most prominent case of astrophysical line emission is that of  $H\alpha$ , in which the electron in a neutral hydrogen atom transitions from the  $n = 3$  to the  $n = 2$  quantum occupation state, emitting a photon with a wavelength of 656 nm, which is in the red part of the visible spectrum.

Filters, although necessary, therefore present an additional challenge when trying to determine stellar spectra accurately. This task is further complicated by the fact that, even in the wavelength range where a filter does detect incoming flux, the fraction of light it detects, known as the transmittance, is not uniform across the range. The transmittance as a function of wavelength is known as a transmission curve, bandpass or filter response function. Examples of response functions for filter systems employed in this project are shown in Figures 2.2-2.3. By comparing these with the filters' infor-

mation in Table 2.2, it can be seen that the exact shape of the response function could have a significant impact on the observed spectrum if not taken into account.

### 1.3 The standard treatment of extinction in observations

In observations, the extinction for a given source is initially unknown. For a stellar population, observers must make use of HR diagram features (absolute magnitudes) that vary as little as possible with variations in age and metallicity. The only known example of this is the red clump (Castellani et al., 1992), representing giant stars sustaining core helium burning. In the HR diagram, these stars form the red terminus of the horizontal branch (HB). Since the age and mass of a star at a given stage in its evolution correlate strongly, the location of the red clump is, by extension, also independent of the masses of its constituent stars. Paczyński & Stanek (1998).

The treatment of extinction in observational surveys is usually via a global extinction value for each filter, such as the constant  $A_X/A_V$  ratios given by Rieke & Lebofsky (1985). This approach has the significant issue of producing  $A_X$  values that do not account for star-to-star variations in flux, which can be several orders of magnitude. As shown in Figure 1.1, the monochromatic flux at a given wavelength varies greatly with effective temperature, as does the ratio between monochromatic fluxes of stars of different temperatures. This makes the notion that stars of different temperatures lose the same flux in a given filter passband, implied by using constant extinction ratios across all stellar classes, inherently flawed. Stars with higher effective temperatures have emission spectra with much higher and (proportionally greater) fluxes at the shorter wavelengths which are most impacted by interstellar extinction. Therefore, it should be expected that hotter stars experience higher extinctions  $A_X$  for a given filter, not equal values.

### 1.4 Empirical extinction curves

Rieke & Lebofsky (1985) found that outside dense molecular clouds, which have high opacities and whose lines-of-sight are less frequently used as a result, all extinction laws for all Johnson filters studied were uniform between wavelengths of 1 and 13  $\mu\text{m}$  when observing sources in the direction of the Galactic Centre. This result was then used to produce constant  $A_X/A_V$  extinction ratios in the same filters. They also determined the now-widely used global average value of 3.08 ( 3.1) for  $R_V = A_V/E(B - V)$ , known as the total-to-selective extinction ratio, for the diffuse ISM.

Cardelli et al. (1989) used observations of mostly O- and B-type main-sequence

stars to produce empirical equations describing the mean ratio of extinction coefficients at a specific wavelength  $\lambda$  ( $A_\lambda$ ) to the extinction in the Johnson- $V$  filter ( $A_V$ ), respectively. From this point onward, this ratio will be referred to as  $A_\lambda/A_V$ . They produced a basic equation of the form:

$$A_\lambda/A_V = a(x) + b(x)/R_V, \quad (1.6)$$

where  $x \equiv 1/\lambda$  and  $R_V \equiv A(V)/E(B-V)$ . The significance of  $R_V$ , as noted in the same paper, comes from its usefulness as an indicator of the nature of the interstellar medium through which the observed light travels in order to reach the observer. The total wavelength range was divided into 4 sub-ranges, each with a governing pair of empirically-determined equations to calculate  $a(x)$  and  $b(x)$ , respectively. This model underpins more recent studies of intrinsic effects on extinction (Girardi et al. (2008), Casagrande & Vandenberg (2018)), and provides the basis for the synthetic  $A_X/A_V$  datasets in this project. Equation 1.6 has become a standard model for theoretical studies to employ for predictions made in the UV, optical and near-IR wavelength regions, although it is not always accurate (O'Donnell (1994), Fitzpatrick (1999)).

O'Donnell (1994) found deviations from the Rieke & Lebofsky (1985) extinction law in the soft-UV spectral range using a sub-sample of 22 stars from the same dataset. This was attributed to the uncertainty in the short-wavelength cutoff of the UV-range Johnson  $U$  filter and to the presence of the Balmer discontinuity within the limits of the filter bandpass.

Fitzpatrick (1999) found that, due to the broadband nature of the Johnson filters and the general decrease of extinction with wavelength, the Cardelli et al. (1989) relations overestimate the extinction in the near-IR and blue-visible Johnson filters. The study put forward corrections to the equations for  $a(x)$  and  $b(x)$  for these wavelength regions. However, in the UV region covered by the Cardelli et al. (1989) equations, the equations are accurate for 93% of a homogeneous UV observational database (Valencic et al., 2004).

Girardi et al. (2008) produced data tables of  $A_X/A_V$  via bolometric corrections (as was carried out in this study). for stellar atmosphere models with parameters  $T_{\text{eff}}$ ,  $\log(g)$  and  $[\text{Fe}/\text{H}]$ . They carried this out using the same ATLAS9 data (Castelli & Kurucz, 2004) that was used to generate the data for this project, but also combined it with data from other studies Girardi et al. (2002), resulting in data covering a parameter space extending beyond the ATLAS9 limits in all three parameters. They used the data tables to calculate the  $A_X/A_V$  values for the stellar models in Padova theoretical isochrones. While determining that the values of  $A_X/A_V$  varied significantly with  $T_{\text{eff}}$  and  $\log(g)$ , the variation with metallicity was found to be 0.17% between  $[\text{Fe}/\text{H}] = 0.0$  and  $[\text{Fe}/\text{H}] = -2.5$ . They found that, when they set  $A_V = 6$ , there was a systematic shift for the ACS system between extinction values calculated star-wise using the BC tables and a constant extinction value. The constant values of  $A_X/A_V$  were calculated



from a yellow dwarf in the low-extinction regime. Overall, the BC tables produced a smaller extinction coefficient in the F814W filter and a larger (F475W-F814W) colour index value. It also caused a change in the shape of the curve at the MSTO. They then applied the BC table data method to the case of the globular cluster M92. They found the optimal metallicity to be  $Z = 0.0004$  ( $[\text{Fe}/\text{H}] \approx -1.6$ ) instead of the value obtained by previous observers of  $Z = 0.0001$  ( $[\text{Fe}/\text{H}] \approx -2.2$ ). Therefore, their use of BC data caused the estimated cluster metallicity to be greater than when using the standard one-size-fits-all approach to extinction.

Casagrande & Vandenberg (2014, 2018a, 2018b) created simple linear models in multiple telescope filter systems, with the output parameter being  $R_X = \frac{A_X}{E(B-V)}$ . This was based on MARCS model stellar atmospheres, which have an upper  $T_{\text{eff}}$  limit of 8000K (Gustafsson et al., 2008). The equation is independent of surface gravity and has the following form:

$$R_X = a_0 + T_4(a_1 + a_2 T_4) + a_3[\text{Fe}/\text{H}] \quad (1.7)$$

where  $T_4 = 10^{-4} \times T_{\text{eff}}$ . The equation is valid for  $5250\text{K} \leq T_{\text{eff}} \leq 7000\text{K}$ . Although these models are mathematically simple (with only 4 coefficients), the limited  $T_{\text{eff}}$  range in which they are applicable is problematic, particularly in the red giant branch and lower main sequence of any stellar population.

## 1.5 Stellar parameters affecting extinction

To understand the significance of differences between stars with respect to interstellar extinction, we must first define the fundamental features of a stellar atmosphere, which will be used in this project as the input variables on which any star-to-star variations in extinction will be modelled.

The effective temperature ( $T_{\text{eff}}$ ) of a star is defined as the thermodynamic temperature of a black body which produces the same stellar flux across all wavelengths (known as the bolometric flux) as that produced by the star. The equation of the radiation emitted by a black body produces the body's flux per unit wavelength per unit angular viewing area,  $F_{\lambda,bb}$ , known as the black body's monochromatic flux. The equation, known as the Planck Law, is as follows:

$$F_{\lambda,bb} = \frac{2hc^2}{\lambda^5 \left( \exp\left(\frac{hc}{\lambda k_B T}\right) - 1 \right)} \quad (1.8)$$

where  $T$  is the thermodynamic temperature of the black body,  $h$  is Planck's constant,  $c$  is the vacuum speed of light and  $k_B$  is Boltzmann's constant. This equation also holds if the light wave frequency is used instead of the wavelength, with the monochromatic flux  $F_{\nu,bb}$  now being the black body flux per unit frequency:

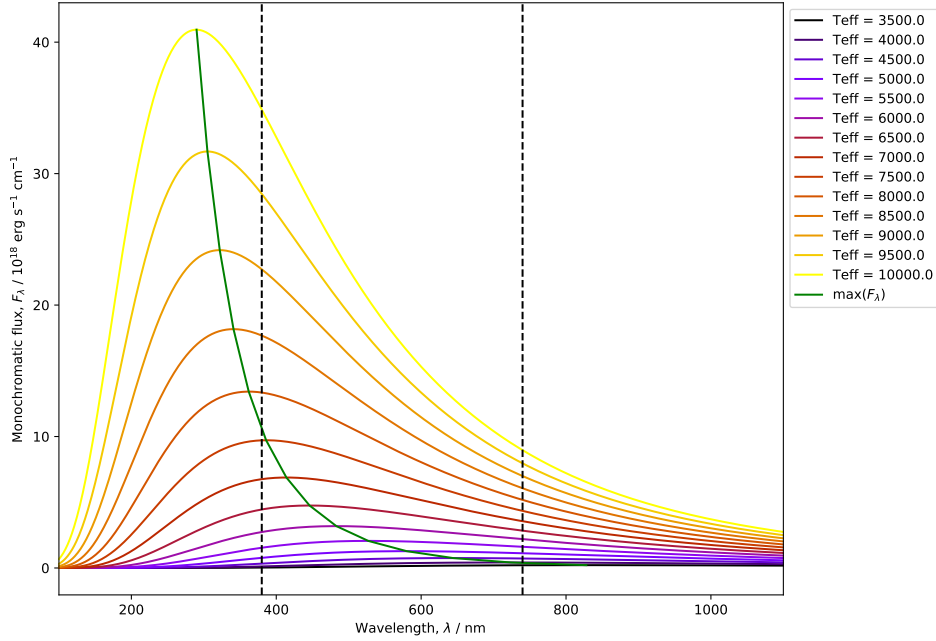


Figure 1.1: Monochromatic flux of a black body for different stellar effective temperatures. The black dashed lines mark the approximate limits of the visible part of the EM spectrum. The green curve represents the distributed of the maxima for the other curves.

$$F_{\nu,bb} = \frac{2h\nu^3}{c^2 \left( \exp\left(\frac{h\nu}{k_B T}\right) - 1 \right)} \quad (1.9)$$

In this project, the definition of monochromatic flux for any given object will be reserved exclusively for the flux per unit wavelength,  $F_{\lambda}$ , with any calculations involving black body fluxes using Equation 1.8.

The general approximation of stars to black bodies (and hence the actual stellar surface temperature to  $T_{\text{eff}}$ ) is valid because all stars have been observed to have spectra that closely resemble those of black bodies, with the notable exception of atmospheric absorption lines. The (intrinsic) luminosity of a star is defined as:

$$L = 4\pi R^2 \sigma_{SB} T_{\text{eff}}^4 \quad (1.10)$$

where  $R$  is the (mean) stellar radius. Effective temperature has an effect on interstellar extinction due to its strong effect on the stellar luminosity and, hence, the flux. For a higher flux, more photons are likely to interact with the ISM, hence a higher extinction coefficient.

The metallicity of a star is defined as the fractional abundance of heavy elements, often approximated by iron (Fe) alone, relative to the star’s hydrogen (H) abundance, compared to that of the Sun. The abundances are determined by the strength of the elements’ characteristic atomic absorption lines in the stellar spectra.

$$[\text{Fe}/\text{H}] = \log \left( \frac{N_{\text{Fe}}}{N_{\text{H}}} \right) - \log \left( \frac{N_{\text{Fe},\odot}}{N_{\text{H},\odot}} \right) \quad (1.11)$$

For a generic atomic species  $E$ ,  $N_E$  represents its number density. For stellar observations,  $N_E$  is measured at the surface. Since the output is logarithmic, a value of  $[\text{Fe}/\text{H}] = 0$  indicates solar metallicity. An increase in metallicity would cause the corresponding absorption lines to be stronger, thus reducing the observable flux. An increased metallicity also implies an increase in abundance of sub-ferrous metals. The presence of more nuclear species, each with unique absorption line configurations, inevitably creates more observable lines, further increasing the apparent extinction in the spectral flux.

The definition of the stellar surface gravity  $g$  is simply the value of the standard Newtonian gravitational acceleration, applied to the stellar surface (the mass is the total stellar mass,  $M_*$ , and the distance is the stellar radius,  $R_*$ ):

$$g = \frac{GM_*}{R_*^2} \quad (1.12)$$

A greater surface gravity, as can be inferred from Equation 1.12, represents a surface with a higher mass density. For stars, being self-gravitating, this infers a higher atomic number density. The effects of surface gravity upon the emitted stellar spectrum arise directly from the effect of atomic number density on the quantum properties of the interactions between the photons and atomic electrons.

When a particle absorption a photon, the absorption process is not instantaneous and therefore carries an uncertainty in the time taken for the process to be completed, with a corresponding uncertainty in energy due to the Heisenberg uncertainty principle. Across a large number of absorptions for the same initial electron state, the result is a spread in the energies of the absorbed photons. The associated emission line is therefore broadened by the multiple wavelengths of the photons. This is universal and referred to as “natural broadening”.

The impact of surface gravity arises via additional broadening effects upon these same absorption lines. When broadening effects are applied to an emission spectrum, such as a spectrum from a stellar surface, the result is that fewer photons pass through the surface, thereby reducing the surface flux seen by an outside observer.

## 1.6 Effects of extinction on interpreting stellar populations

The goal of this project is to compare different extinction treatments and the subsequent effect on the interpretation of observational cluster datasets. For any observational set of stars, the stars' extinction coefficients will be completely unknown from the data alone. In order to compare observational and theoretical data, the most convenient approach is to add the (theoretical) extinction coefficient(s) to the theoretical dataset magnitudes (i.e., absolute magnitudes), before comparing to the distance-corrected observational data. As a result, the quantity from each dataset that is being compared is the absolute magnitude plus the extinction coefficient. If we label this quantity  $M_{\text{ext},X}$  for a given filter, we can define it as:

$$\begin{aligned} M_{\text{ext},X} &= M_X + A_X \text{ (theoretical data)} \\ &= m - (m - M)_{X,0} \text{ (observational data)} \end{aligned} \tag{1.13}$$

However, as noted earlier, in astronomy it is not feasible to attempt observations by a single instrument at all wavelengths. Telescopes instead are purpose-built to study a single wavelength range within the full EM spectrum. Within this range, telescope observation ranges are further divided by filters or passbands, one of which is placed on their aperture at any given observation time. As shown in Figures 2.3-2.2, any single filter  $X$  has a limited range of wavelengths for which it is able to detect flux. It can also be seen in these figures that the transmittance of the filter changes as a function of wavelength. These instrumental factors must be considered, in addition to the observational challenges of distance and interstellar extinction, in order to correctly analyse observation telescope data.

If we compare the individual black body spectra in Figure 1.1, it can be seen that the maximum monochromatic flux of the black body occurs at an increasingly shorter wavelength for objects with increasingly higher temperatures. This makes the object appear bluer to an observer. The relationship between the wavelength at which the monochromatic flux is maximal ( $\lambda_{\text{max}}$ ) and the black body temperature is quantified by Wien's displacement law:

$$\lambda_{\text{max}} T = 2.898 \times 10^6 \text{ nm K} \tag{1.14}$$

More importantly, for two wavelength regions which are sufficiently far apart, the change in flux between the regions is always greater for stars with higher effective temperatures. Therefore, to measure a star's effective temperature, observers compare the star's observed flux in two filters operating at different wavelengths within the UV-IR wavelength range. The difference between the star's flux magnitudes in each of the two filters is then taken, with the flux in the redder filter being deducted from that of the bluer filter. This quantity is known as the colour index. For two filters  $X$  and  $Y$ ,

with  $X$  being bluer than  $Y$ , the colour index of observations made using those filters,  $(X - Y)$ , is defined as:

$$\begin{aligned}(X - Y) &= m_X - m_Y \\ &= (m_{X,0} - m_{Y,0}) + (A_X - A_Y) \\ &= (X - Y)_0 + E(X - Y)\end{aligned}\tag{1.15}$$

where  $(X - Y)_0$  is the true or intrinsic colour index of the object and  $E(X - Y) = A_X - A_Y$  is known as the colour excess, but can also be denoted in literature using the term “reddening”. A major advantage of using the intrinsic colour index over absolute magnitudes is that it is completely independent of distance. The colour excess represents the effect of extinction on the observed colour index. Its importance arises from the prominence of the intrinsic colour index in determining effective temperature. Higher values of  $(X - Y)$  indicate redder stars, with lower effective temperatures.

The most commonly-used colour index, employed as a reference for most optical observations, is the Johnson  $(B - V)$  index. This is due to these filters being the among most long-lived, well-used and best-studied available, allowing for better comparisons of different data, including data from older archives.

Due to the potential confusion due to the use of the term “reddening” for both  $A_X$  and  $E(X - Y)$  in literature,  $A_X$  will be referred to here as the “extinction” or “extinction coefficient” and  $E(X - Y)$  as the “colour excess”.

## 1.7 Project objective

The goal of this project is to attempt to use analytic functions to model the variation of the extinction coefficients in multiple photometric filter systems, across as large a range of stellar types as possible, with the ultimate goal of using this simplification of the variations to determine the differences in the estimated optimal ages, elemental abundances (known collectively in astronomy as metallicity) and extinction reference values of stellar populations (i.e., star clusters) from the current standard method for simulating extinction. If such differences exist and if they are of significant size, it could cause a recalculation of the properties of observed star clusters. This could potentially cause a reinterpretation of these clusters’ history, including where and when they formed in the Milky Way and the chemical enrichment of the gas that formed their stars.

# Chapter 2

## Methodology

### 2.1 Calculating extinction ratio data

All the equations in Section 1.6, including those for extinction, are not useful when applied to telescopes, as any filter will only detect a small fraction of the bolometric stellar flux that reaches the telescope. The missing information resulting from this observational constraint renders it difficult to determine the interstellar extinction. These constraints must be mitigated before an accurate value of the extinction coefficient can be determined. This mitigation is carried out by calculating corrections.

The use of bolometric corrections requires the detailed knowledge of stellar spectra least susceptible to significant extinction, i.e., nearby stars with high apparent fluxes. Only with complete knowledge of the spectrum from a reference star can the true spectrum of a distant star with unknown extinction be calculated. The spectra of these stars can be computed by using a grid of predicted fluxes from a stellar atmosphere model, the grid being composed of the stellar parameters known to change emission in stellar atmospheres. These are effective temperature, surface gravity and metallicity. For all filter systems studied in this project, the nearby bright star Vega ( $\alpha$  Lyr) was used as the reference object. Using Vega as the reference star is the most well-known approach to photometric calibration (Casagrande & VandenBerg, 2014).

After accounting for the effect of interstellar extinction on an object's emission, its apparent magnitude in the wavelength range of a given filter  $X$ , defined as increasing from the shortest ( $\lambda_1$ ) to the longest ( $\lambda_2$ ) wavelength for which its response function is non-zero, can be calculated as:

$$m_X = -2.5 \log_{10} \left( \frac{\int_{\lambda_1}^{\lambda_2} f_\lambda (10^{-0.4A_{X,\lambda}}) S_\lambda d\lambda}{\int_{\lambda_1}^{\lambda_2} f_\lambda^0 S_\lambda d\lambda} \right) + m_X^0 \quad (2.1)$$

where  $f_\lambda$  represents the (theoretical) monochromatic flux at a given wavelength  $\lambda$  at the observer distance from the source,  $A_{X,\lambda}$  is the extinction coefficient in  $X$  as

a function of wavelength and  $S_\lambda$  represents the filter response function of  $X$ .  $f_\lambda^0$  and  $m_X^0$  represent the monochromatic flux and apparent magnitude, respectively, in  $X$  of a known reference object, which is Vega in the case of this project.

To derive the equation linking a bolometric correction with the extinction parameter, we start with the definition of a bolometric correction in a filter  $X$ , which is denoted by  $BC_X$ :

$$BC_X \equiv M_{\text{bol}} - M_X \quad (2.2)$$

where  $M_X$  is the absolute magnitude of the object in  $X$  and  $M_{\text{bol}}$  is its (predicted) absolute bolometric magnitude, defined relative to the Sun using:

$$M_{\text{bol}} = M_{\text{bol},\odot} - 2.5 \log_{10} \left( \frac{4\pi R^2 F_{\text{bol}}}{L_\odot} \right) \quad (2.3)$$

where  $F_{\text{bol}}$  is the bolometric stellar flux at its surface,  $R$  is the stellar radius,  $M_{\text{bol},\odot}$  is the solar absolute bolometric magnitude, which is assumed in this work to have a value of 4.75 and  $L_\odot$  is the solar luminosity, for which a value of  $3.844 \times 10^{33} \text{ erg s}^{-1}$  is used. Bolometric corrections can be expressed as a function of extinction using the definition of  $M_X$  in terms of  $m_X$  and the distance  $d$  to the source:

$$M_X = m_X - 2.5 \log_{10} \left( \left( \frac{d}{10 \text{ pc}} \right)^2 \right), \quad (2.4)$$

together with the equation  $f_\lambda d^2 = F_\lambda R^2$ , where  $F_\lambda$  is the monochromatic flux at  $\lambda$  at the stellar surface. This gives the final function for a bolometric correction for filter  $X$ :

$$\begin{aligned} BC_X = M_{\text{bol},\odot} - m_X^0 - 2.5 \log_{10} \left( \frac{4\pi R^2 F_{\text{bol}}}{L_\odot} \right) \\ + 2.5 \log_{10} \left( \frac{\int_{\lambda_1}^{\lambda_2} F_\lambda (10^{-0.4A_{X,\lambda}}) S_\lambda d\lambda}{\int_{\lambda_1}^{\lambda_2} f_\lambda^0 S_\lambda d\lambda} \right) \end{aligned} \quad (2.5)$$

For a filter  $X$ , the extinction parameter  $A_X = A_{X,\lambda}$  must be calibrated relative to a known value. In this work we will input a value of the extinction in the well-studied Johnson- $V$  filter,  $A_V$ . To extract  $A_X$ , we use the simple relation:

$$A_{X,\lambda} = \left( \frac{A_{X,\lambda}}{A_V} \right) A_V \quad (2.6)$$

together with the chosen value of  $A_V$  (for this project the values were  $A_V = 0, 1$  - note that  $BC_X(A_V = 0)$  essentially assumes no extinction in any filter), before taking the difference between the two  $BC_X(A_V)$  outputs, giving the following equation (Girardi et al., 2008):

$$BC_X(0) - BC_X(A_V) = (A_X/A_V) A_V \quad (2.7)$$

As demonstrated in the equation above, any dependence of the  $A_X/A_V$  data on the Vega measurements or (as yet unknown or uncertain) bolometric quantities from Equation 2.5 is eliminated during the subtraction.

Once the data  $A_X/A_V$  was calculated, analytical model templates of the three stellar parameters described in Section 1.5 were created and applied to the data, with the best-fit model coefficients being calculated using a least-squares fit algorithm.

## 2.2 Software used

To generate the predicted stellar flux, the ATLAS9 model stellar atmosphere code (Kurucz, 1993) was used to produce monochromatic fluxes for a series of wavelengths ranging from 9 nm to 160,000 nm, with a resolution of 2 nm or less in the UV. Table 1 of Castelli & Kurucz (2004) contains precise details of the coverage in  $(T_{\text{eff}}, \log(g))$  parameter space, while a brief summary of the limits of the space is listed in Table 2.1. Four input metallicities were used for ATLAS9, at values of  $[\text{Fe}/\text{H}] = -2, -1, 0$  and 0.5, covering the metallicities of most observed globular and open clusters. Each metallicity case was subject to the same coverage in ATLAS9. As shown in Figure 2.1, with the exception of the coolest, and therefore faintest, main sequence stars in the bottom right of the figure, the ATLAS9 grid covers the required parameter space for isochrones of all ages. The variation of isochrones at the plotted ages with metallicity is not significant with respect to the grid coverage.

The tables of bolometric corrections were generated using a FORTRAN 77 code incorporating the steps described in Section ??, inputs with tables describing the response functions of all three filter systems at the same wavelengths as those listed in the ATLAS9 model atmosphere tables, with the number of tables for each stellar metallicity value equal to the total number of  $(T_{\text{eff}}, \log(g))$  combinations available.

Once the bolometric correction tables were produced, all subsequent processes were written in Python 2.7 in the form of an IPython notebook. The repository containing all data, plots and programme codes for this project can be found at [https://github.com/AlexlwAstro/phd\\_work](https://github.com/AlexlwAstro/phd_work).

The isochrones used were generated using the latest Bag of Stellar Tricks and Isochrones (BaSTI) web interface (Pietrinferni et al. (2004), Hidalgo et al. (2018)). The filter systems whose throughput data were employed by BaSTI to generate the fluxes for the isochrones were ACS, WFC3 and Gaia-DR2. It should be noted that the



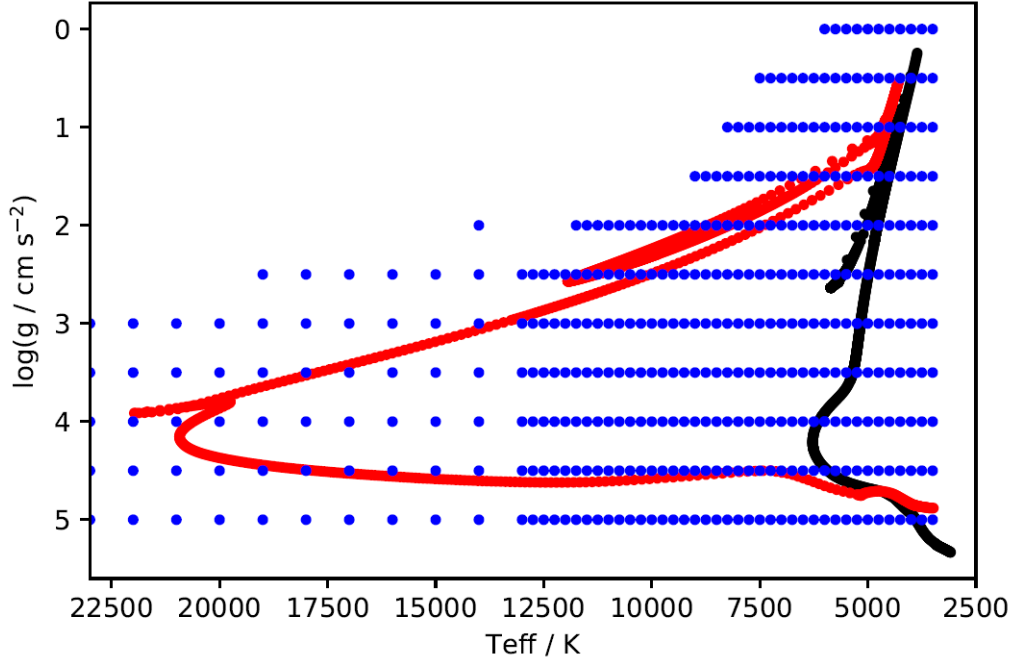


Figure 2.1:  $T_{\text{eff}}$ - $\log(g)$  scatter plot for a BaSTI 50 Myr,  $[\text{Fe}/\text{H}] = -1$  isochrone (red), a BaSTI 12 Gyr,  $[\text{Fe}/\text{H}] = -1$  isochrone (black) and ATLAS9 model grid (blue) for  $T_{\text{eff}} \leq 23000$  K.

| Parameter / unit             | Minimum | Maximum | Number of values |
|------------------------------|---------|---------|------------------|
| $T_{\text{eff}} / \text{K}$  | 3500    | 50000   | 76               |
| $\log(g / \text{cm s}^{-2})$ | 0.0     | 5.0     | 11               |
| $[\text{Fe}/\text{H}]$       | -2.0    | 0.5     | 4                |

Table 2.1: Ranges for the input parameters for ATLAS9 atmospheric models

WFC3 isochrone output for BaSTI does not include flux magnitudes for the F300X filter.

## 2.3 Filters studied

In this project, three broad-band filter systems were employed. Two are systems on board the Hubble Space Telescope (HST). These are the Advanced Camera for Surveys (ACS), installed in 2002 on the HST (Sarajedini et al., 2007), and the Ultraviolet Imaging Spectrograph channel of the Wide-Field Camera 3 (WFC3/UVIS), installed on the HST in 2009 (Kalirai et al. (2010), MacKenty et al. (2010)). The third is the single set of three broadband filters mounted on the Gaia space observatory (Jordi et al., 2010), launched in 2013.

Reference will also be made to the Johnson-Morgan filter system (often simply known as the Johnson system) UBV Johnson & Morgan (1953), later extended as the Johnson-Cousins UBVRI Bessell (1990) system, which has been in use for decades and continues to be the standard reference for more modern filter systems. Of particular importance are the Johnson blue ( $B$ ) and yellow ( $V$ ) filters, as these formed the original benchmark for observing stellar populations and evolutionary stages.

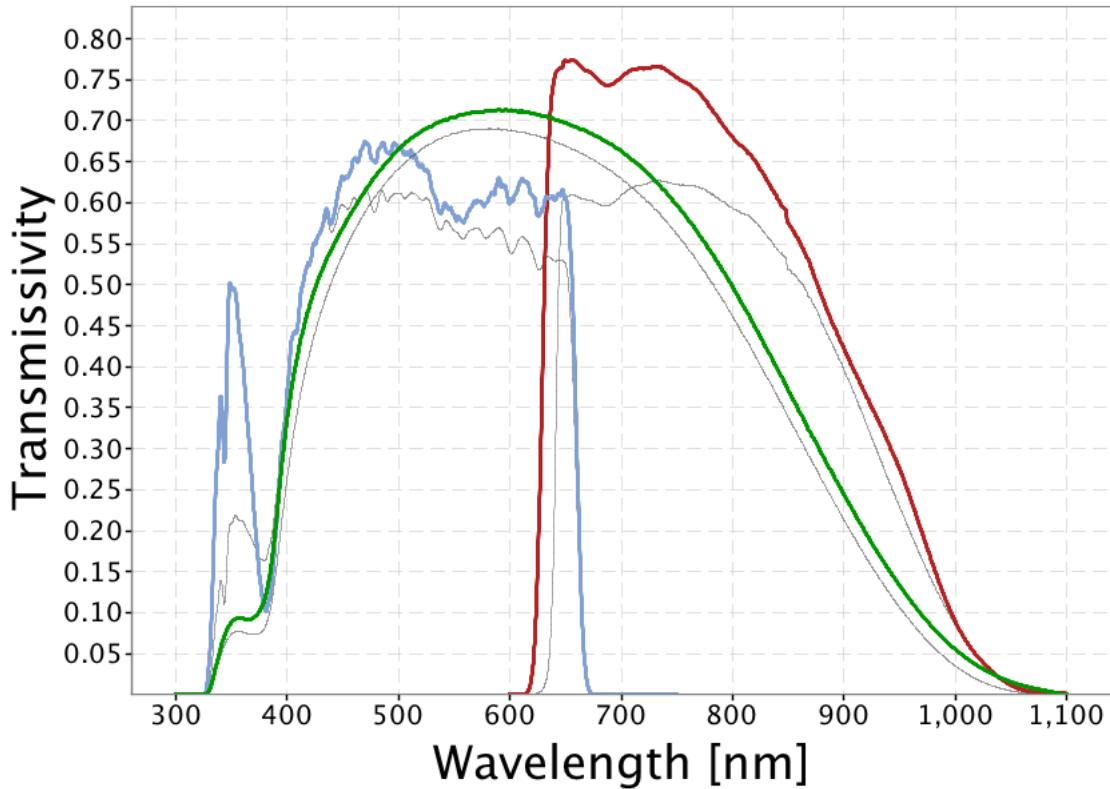


Figure 2.2: Filter response functions for Gaia photometric filters. Source: [https://www.cosmos.esa.int/web/gaia/iow\\_20180316](https://www.cosmos.esa.int/web/gaia/iow_20180316)

The standard treatment of extinction is to apply a single constant value of the extinction coefficient for a given filter  $X$ , denoted in the literature by  $A_X$ . For wavelengths in or around the optical spectral range, this quantity is usually expressed as a fixed ratio of the (constant) coefficient value in the Johnson- $V$  filter, the standard visual comparison filter. The wavelengths of optical light typically range between 3800 Å and 7400 Å.

In Table 2.2, all the filters used for this project are listed. The name of each filter is displayed alongside its central wavelength ( $\lambda_{\text{cen}}$ ), full-width at half-maximum (FWHM) and the minimum ( $\lambda_{\text{min}}$ ) and maximum ( $\lambda_{\text{max}}$ ) detection wavelengths. Hence, when

| System | Filter          | $\lambda_{\text{cen}} / \text{\AA}$ | FWHM / $\text{\AA}$ | $\lambda_{\text{min}} / \text{\AA}$ | $\lambda_{\text{max}} / \text{\AA}$ |
|--------|-----------------|-------------------------------------|---------------------|-------------------------------------|-------------------------------------|
| ACS    | F435W           | 4359                                | 881                 | 3610                                | 4860                                |
|        | F475W           | 4781                                | 1403                | 3863                                | 5563                                |
|        | F555W           | 5413                                | 1236                | 4584                                | 6209                                |
|        | F606W           | 5961                                | 2255                | 4634                                | 7180                                |
|        | F625W           | 6323                                | 1390                | 5446                                | 7100                                |
|        | F775W           | 7763                                | 1517                | 6804                                | 8632                                |
|        | F814W           | 8117                                | 2096                | 6885                                | 9648                                |
| WFC3   | F218W           | 2216                                | 329                 | 1990                                | 2603                                |
|        | F225W           | 2341                                | 464                 | 1990                                | 2968                                |
|        | F275W           | 2696                                | 417                 | 2282                                | 3119                                |
|        | F300X           | 2722                                | 660                 | 2137                                | 4098                                |
|        | F336W           | 3368                                | 550                 | 3014                                | 3707                                |
|        | F390W           | 3929                                | 951                 | 3255                                | 4470                                |
|        | F438W           | 4322                                | 674                 | 3895                                | 4710                                |
|        | F475W           | 4768                                | 1482                | 3942                                | 5582                                |
|        | F555W           | 5262                                | 1578                | 4381                                | 7045                                |
|        | F606W           | 5941                                | 2298                | 4700                                | 7204                                |
|        | F625W           | 6274                                | 1573                | 5414                                | 7138                                |
|        | F775W           | 7725                                | 1454                | 6869                                | 8571                                |
|        | F814W           | 7814                                | 1505                | 6978                                | 9684                                |
| Gaia   | G               | 6631                                | 4397                | 3321                                | 10515                               |
|        | G <sub>bp</sub> | 5330                                | 2530                | 3283                                | 6714                                |
|        | G <sub>rp</sub> | 7896                                | 2956                | 6296                                | 10637                               |

Table 2.2: Basic properties of the filters employed in this project. See text for details. Source: <http://svo2.cab.inta-csic.es/svo/theory/fps3/index.php>

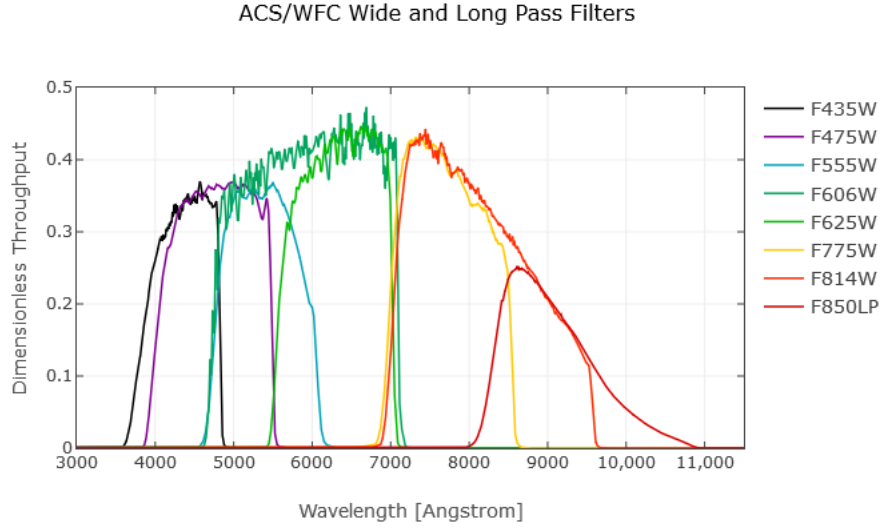


Figure 2.3: Filter response functions for wide-field ACS filters. Source: <http://www.stsci.edu/hst/acs/analysis/throughputs>

combined, these filters cover wavelengths from the soft-ultraviolet (soft-UV) to the near-infrared (NIR), including all visible wavelengths. The FWHM is defined as the difference between the lowest and highest wavelength values at which the transmittance value is half of its maximum value for the filter, typically assuming the response function can be approximated as a Gaussian distribution centred on the central wavelength. The FWHM acts as an approximate measure of the wavelength range within which the filter can reliably be used for observations.

## 2.4 Isochrone data fitting

To obtain isochrones from the BaSTI online database, the desired age range, initial metallicity and filter system must be specified. Therefore, the values of these quantities are shared by all stellar objects. For the stages in stellar evolution prior to the main-sequence turn-off, any changes in atmospheric metallicity are insignificant, due to the factors discussed in Section ??.

The output from the BaSTI database for each model stellar object gives the model's initial mass and current mass (i.e. after a time equal to the isochrone age), together with the logarithms of the stellar luminosity in solar units ( $\log(L/L_{\odot})$ ) and of the effective temperature in K ( $\log(T_{\text{eff}})$ ), followed by the absolute magnitudes (with zero extinction) of the object in each filter of the system. To derive the surface gravity  $g$ , we

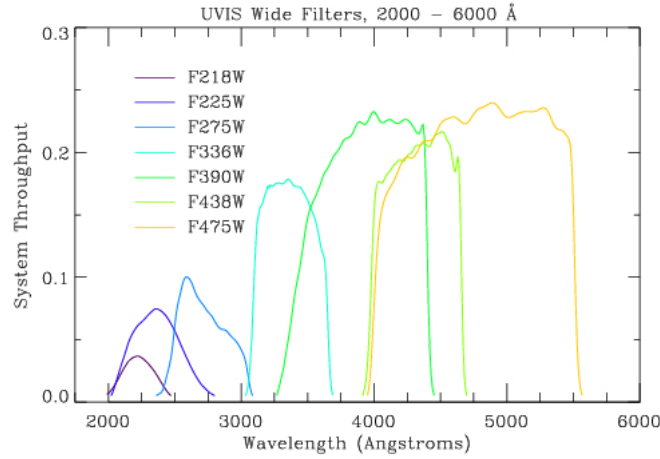


Figure 2.4: Filter response functions for wide-field WFC3 filters. Source: [http://www.stsci.edu/hst/wfc3/ins\\_performance/throughputs/UVIS\\_filterthru.html](http://www.stsci.edu/hst/wfc3/ins_performance/throughputs/UVIS_filterthru.html)

| Isochrone<br>(Age/Myr , [Fe/H]) | $T_{\text{eff}}$<br>minimum | $T_{\text{eff}}$<br>maximum | $\log(g)$<br>minimum | $\log(g)$<br>maximum |
|---------------------------------|-----------------------------|-----------------------------|----------------------|----------------------|
| 500,0.002                       | 2870                        | 9640                        | 0.886                | 5.137                |
| 1000,0.002                      | 2824                        | 8035                        | 1.608                | 5.184                |
| 5000,-1.049                     | 3118                        | 7112                        | 0.456                | 5.318                |
| 10000,-1.049                    | 3086                        | 6412                        | 0.286                | 5.332                |

Table 2.3: Ranges of effective temperature and surface gravities in selected BaSTI isochrones

must combine Equation 1.10, to derive the stellar radius, and Equation 1.12. Equation 2.8 shows the resultant definition of  $g$ :

$$g = \frac{4\pi GM_* \sigma_{\text{SB}} T_{\text{eff}}^4}{L_*} \quad (2.8)$$

After this had been completed, each object had a co-ordinate in  $(T_{\text{eff}}, \log(g))$  parameter space, plus the metallicity of the overall isochrone model. The filter magnitudes in the photometric data are the apparent magnitudes of the stars assigned to NGC 6793. Therefore, to match the quantities of the observational and isochrone datasets being compared, it was necessary to correct the observational data for distance and add extinction to the isochrones. This is that standard procedure used when analysing observational data. Thus, we were comparing the  $M_{\text{ext},X}$  values for the isochrones and the observational data. The functions described in Section 3.1 were then applied to the dataset of stellar objects, producing values of  $M_{\text{ext},X}$  for each filter for all objects, as is the standard for analysing observational data with unknown extinction coefficients.

When comparing the two approaches to extinction, in order to test for any differ-

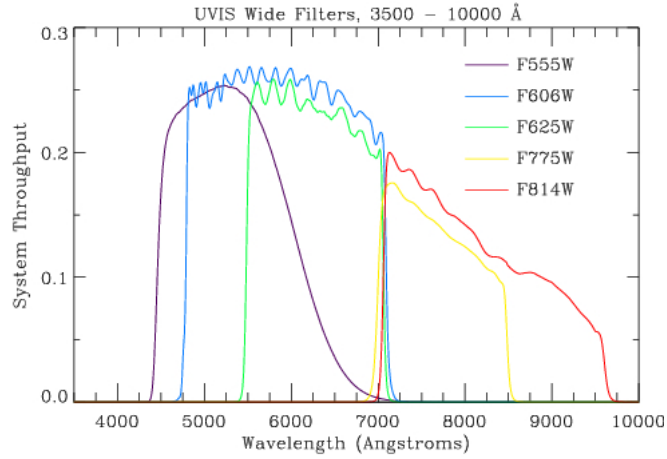


Figure 2.5: Filter response functions for wide-field WFC3 filters. Source: [http://www.stsci.edu/hst/wfc3/ins\\_performance/throughputs/UVIS\\_filterthru.html](http://www.stsci.edu/hst/wfc3/ins_performance/throughputs/UVIS_filterthru.html)

ences in projected isochrone age via the MSTO, a range of ages must be considered. A “primary” age was utilised as the true cluster isochrone age. This primary isochrone was subjected to both the function-based (FBEC) and standard extinction-coefficient approaches. Two isochrones with ages equidistant from the primary were subjected to the standard approach only. All four of the resulting  $M_{\text{ext},X}$  isochrones were plotted together in the four chosen CMD axes, together with the original (zero-extinction) isochrone for visual reference.

This procedure was employed for two values of  $A_X/A_V$  for the standard (fixed) extinction treatment. Both were extracted from the ATLAS9 data tables for a  $\log(g)$  value of 5.0 to represent a main-sequence star, highly desirable when comparing MSTO positions. Given the large number of filters studied in this project, four commonly-used CMD axes were selected to test for any effects of a function-derived  $A_X$ . Two of these are specific to the WFC3 system, with one CMD each for ACS and Gaia.

## 2.5 Observational test case: NGC 6793

To test the effects of the two different treatments of  $A_X/A_V$  on observational data, both were employed to predict the isochrone parameters (age,  $[\text{Fe}/\text{H}]$  and  $A_V$ ) for the open cluster NGC 6793.

NGC 6793 has little information available in the literature when compared to open clusters. Two observational studies have been published which give estimates for the properties of the cluster. Both sets of results are listed in Table 2.4.

The Gaia DR2 dataset for NGC 6793, containing the parallaxes and apparent mag-

| Cluster property       | K05              | GC18                           |
|------------------------|------------------|--------------------------------|
| Distance modulus / mag | 10.73            | 8.894                          |
| -> distance / pc       | 1400             | 601                            |
| log(age / yr)          | 8.64             | 8.78                           |
| -> Age / Myr           | 437              | 603                            |
| $E(B - V)$ / mag       | 0.17             | 0.272                          |
| $[Fe/H]$               | ?                | ?                              |
| Members                | ? (> 3 ACSS-2.5) | 465 (271 with Gaia photometry) |

Table 2.4: Observational parameters for NGC 6793, according to Kharchenko et al. (2005) (WEBDA archive page) and Gaia Collaboration et al. (2018)

nitudes (in all three Gaia filters) for 338 objects identified as belonging to the cluster, was obtained. The number of objects is greater than the 271 photometric Gaia objects found by Gaia Collaboration et al. (2018). In addition to this, there were significant variations in the observed parallaxes of individual stars, far beyond the maximum cluster radii expected (Schilbach et al. (2006)). Some objects were even assigned negative parallax values, which are therefore mathematically impossible. Restrictions on the parallax measurements were implemented, by imposing a distance-based selection range centred at 600 pc, which was treated as the centre of the cluster, in line with the Gaia Collaboration et al. (2018) estimate in Table 2.4. The range was decreased until the remaining sample size was approximately equal to 271. When this was implemented, the final sample of observational data for NGC 6793 contained 274 objects. Some of these objects still had parallax distances further from the cluster centre than would be expected for any star cluster. The size of the final dataset balanced the need for maintaining sufficient data points, to achieve a valid comparison to the previous studies of NGC 6793, and eliminating anomalous data.

The isochrone fitting to the NGC 6793 was done by eye using a plot of the cluster’s observed Gaia CMD, the position of each star corrected for its parallax distance. Using the values of  $E(B - V)$  and age from Gaia Collaboration et al. (2018), a standard-case isochrone was derived, again assuming a diffuse ISM (i.e.,  $R_V = 3.1$ ). The standard treatment was employed twice, creating a different isochrone each time. A coefficient calculated from  $(A_X/A_V)_{MS}$  was applied in one case and one calculated using  $(A_X/A_V)_{plat}$  in the other. The fitting process was carried out in sequential stages:

1. First, the upper main sequence of the FBEC isochrone was fitted to that of the standard-case isochrone by varying the value of  $A_V$  used to calculate the final FBEC value for each stellar object.
2. Next, the age of the FBEC isochrone was varied to match the observed turn-off location in the NGC 6793 data as far as possible.

3. Finally, the FBEC isochrone metallicity was varied in an attempt match the observed lower main-sequence.

The isochrone with the resulting parameters were then plotted alongside two standard-case isochrones, The resulting curves were compared to each other for accuracy with respect to the observational data.



# Chapter 3

## Results and discussion

### 3.1 Extinction coefficient models

A property found in the data for some filters, more pronounced at higher metallicity but with a possible slight dependence on surface gravity, is the tendency of the gradient of  $A_X/A_V$  with increasing  $T_{\text{eff}}$  to become significantly less positive at the lowest temperatures in the data, typically 4000K and below. The spread in  $A_X/A_V$  values for different  $\log(g)$  is typically about 0.2-0.4, with a linear progression from  $\log(g) = 5.0$  at the lowest end to  $\log(g) = 0.0$  at the highest. In some filters, at the highest metallicity employed ( $[\text{Fe}/\text{H}] = 0.5$ ), this phenomenon causes the gradient to invert and become significantly negative, reversing the trend everywhere else in the data, including for the same filters at lower metallicity. Due to the shape of the resulting point-to-point line in these axes, it has been dubbed the “tail-flick” phenomenon. This was ignored as an artefact from the numerical integration required for Equation 2.5. This was due to the physical infeasibility of a cooler star experiencing a higher extinction  $A_X$  for a globally-constant  $A_V$  value and metallicity, as was assumed for data in each BC table. In the relevant filters, only effective temperatures above those affected by the gradient inversion was used for fitting.

In order to find usable functions without running into issues with degeneracy between coefficients, the three input stellar parameters prioritising which parameters to model first, before expanding the function to include parts modelling the impact of other parameters and their associated coefficients. Too many coefficients created errors that were significantly greater in degenerate coefficients than in non-degenerate ones. This would obscure any useful information about the validity of the function form.

The bolometric flux of a black body can be calculated as the total area under the curve described by the Planck function per unit wavelength/frequency as a function of wavelength/frequency. Since stellar emission spectra can be reasonably approximated by a black body emission with absorption lines, it can be seen from Equation 1.10 that the greatest effect on stellar spectra, and therefore on the extinction coefficient, will

come from effective temperature. Therefore, the initial functions to be fitted were simple analytical functions of  $T_{\text{eff}}$  only:

$$A_{\text{pow}}(T_{\text{eff}}) = a(T_4)^b + c \quad (3.1)$$

$$A_{\text{exp}}(T_{\text{eff}}) = a \exp(bT_4) + c \quad (3.2)$$

where  $T_4 = 10^{-4} \times T_{\text{eff}}$ . The fitting operation was carried out on the data for solar metallicity ( $[\text{Fe}/\text{H}] = 0.0$ ) and, because it gave the greatest number of  $T_{\text{eff}}$  data points,  $\log(g) = 5$ . This dataset will be referred to as the basic fitting data (BFD).

For the data in the Gaia filters, the opportunity was taken to compare the model for  $R_X$  and coefficients detailed for these filters by Casagrande & Vandenberg (2018). To apply their model to the extinction ratios used for this project, the definition of  $R_X$  was used to construct the following equation:

$$\frac{A_X}{A_V} = \frac{R_X}{R_V} = \frac{R_X}{3.1} \quad (3.3)$$

There were filters whose BFD could not support an accurate fit or maintain the desired accuracy across all combinations of  $\log(g)$  and  $[\text{Fe}/\text{H}]$  using  $A_{\text{pow}}$  or  $A_{\text{exp}}$ . For these filters, more intricate functions were sought, including functions with explicit dependences on  $g$  and  $[\text{Fe}/\text{H}]$ . Several unsuccessful approaches were made before an acceptable function was found for each filter.

The most successful approach was plotting all the available data for each filter, in multiple 2D and 3D axes, and analysing it visually. The trends seen in the data were transcribed to find not only an overarching function template, akin to the status of  $A_{\text{pow}}$  and  $A_{\text{exp}}$ , but also smaller mathematical constructs within the template, such as describing a decay coefficient in terms of  $\log(g)$  and  $[\text{Fe}/\text{H}]$ . The details of the final form of the template as a function of each stellar parameter were deduced by fitting a logistic function of  $T_{\text{eff}}$  to the  $A_X/A_V$  data for each ( $[\text{Fe}/\text{H}], \log(g)$ ) combination. This was decided on the basis that  $A_{\text{exp}}$  had been superior to  $A_{\text{pow}}$  in describing the data for all relevant filters and because, for these filters, the low- $T_{\text{eff}}$  change in gradient appeared to be more significant than for others and the gradient was not inverted, as can be seen in Figures ??-??. This is still the case, even after accounting for the difference in  $A_X/A_V$  scale between filters. In particular, the  $T_{\text{eff}}$  gradient prior to the plateau appears to lead to an asymptote at lower, but still physically-viable, temperatures. This issue is resolved by the logistic function's property of converging to a constant value for both very high and low values of the input variable.

For a general logistic function in  $T_{\text{eff}}$ , there are four principle parameters:

- The global maximum value, denoted in this case by  $A_{\text{max}}$ ;
- The global minimum value,  $A_{\text{min}}$ ;

- The exponential decay coefficient,  $k$ ;
- The  $T_{\text{eff}}$ -coordinate of the sigmoid midpoint, in this case  $T_0$ .

It was confirmed that this new function could describe each scenario accurately enough for further analysis. The resulting coefficients were tabulated and analysed for trends and, if found, the nature of those trends. This allowed for the incremental construction of sub-functions of  $\log(g)$  and  $[\text{Fe}/\text{H}]$ , making the overall function,  $A_{\text{logis}}$ , sensitive to all three input stellar atmosphere parameters, with effective temperature having the greatest effect and the relative effects of the other parameters dependent on the best-fit values of the relevant coefficients.

The sub-functions of  $\log(g)$  and  $[\text{Fe}/\text{H}]$ , upon inspection of the coefficients for the  $T_{\text{eff}}$ -only logistic function, were found to be simple functions of  $\log(g)$  and  $[\text{Fe}/\text{H}]$ , independent of  $T_{\text{eff}}$  variations. This allowed for them to be used as the definitions of  $T_0$  and  $k$ , as shown in Equations 3.4 and 3.5, respectively.

$$T_0 = a \log(g) + b \left( \frac{[\text{Fe}/\text{H}]}{|[\text{Fe}/\text{H}]|^{1/2}} \right) + c \quad (3.4)$$

$$k = d \log(g) + e [\text{Fe}/\text{H}] + f \quad (3.5)$$

$$A_{\text{logis}}(T_{\text{eff}}, g, [\text{Fe}/\text{H}]) = \frac{(A_{\text{max}} - A_{\text{min}})}{(1 + \exp(-10^{-4}k(T_{\text{eff}} - T_0)))} + A_{\text{min}} \quad (3.6)$$

The final form was then subjected to a final fit on the entire  $A_X/A_V$  dataset, covering the entire  $(T_{\text{eff}}, \log(g), [\text{Fe}/\text{H}])$  parameter space available.  $A_{\text{logis}}$  was able to accurately reproduce the behaviour of almost the entire dataset. The details are given in \*\*\*\*.

The extinction-ratio data for all filters, with the exception of the four fully-UV filters in the WFC3 system, could be accurately modelled by the simplest functions trialled for fitting,  $A_{\text{pow}}(T_{\text{eff}})$  or  $A_{\text{pow}}(T_{\text{eff}})$ .

All the functions are consistent with the general trends predicted by the physics in stellar atmospheres, since the effective temperature has the greatest effect upon the value of  $A_X/A_V$ , with relatively minor differences due to \*\*\*\*

## 3.2 Effect on isochrones

The ATLAS9 metallicity chosen for calculating the fixed-extinction  $A_X/A_V$  values to be applied to the isochrone was that which best matched the metallicity of the isochrone to which the coefficient was applied. The ATLAS9 value will be denoted  $[\text{Fe}/\text{H}]_{\text{CM}}$ . The first value was equal to  $(A_X/A_V)_{\text{plat}} = (A_X/A_V)(T_{\text{eff}} = 50,000\text{K}, \log(g) = 5.0, [\text{Fe}/\text{H}]_{\text{CM}})$ , and the second was equal to  $(A_X/A_V)_{\text{MS}} = (A_X/A_V)(T_{\text{eff}} = 5,000\text{K}, \log(g) = 5.0, [\text{Fe}/\text{H}]_{\text{CM}})$ .

| System | Filter          | Function<br>( $A_{\text{pow}}$ or $A_{\text{exp}}$ ) | Coefficients         |                      |                     |
|--------|-----------------|------------------------------------------------------|----------------------|----------------------|---------------------|
|        |                 |                                                      | $a$                  | $b$                  | $c$                 |
| ACS    | F435W           | pow                                                  | $-0.0276 \pm 0.0061$ | $-0.967 \pm 0.1918$  | $1.3613 \pm 0.005$  |
|        | F475W           | pow                                                  | $-0.0235 \pm 0.0042$ | $-1.2855 \pm 0.174$  | $1.2323 \pm 0.0032$ |
|        | F555W           | pow                                                  | $-0.0089 \pm 0.0034$ | $-1.534 \pm 0.3895$  | $1.0473 \pm 0.0026$ |
|        | F606W           | exp                                                  | $-0.2295 \pm 0.0361$ | $-2.9413 \pm 0.3326$ | $0.9591 \pm 0.0017$ |
|        | F625W           | exp                                                  | $-0.0741 \pm 0.0487$ | $-3.3839 \pm 1.4339$ | $0.8647 \pm 0.0016$ |
|        | F775W           | exp                                                  | $-0.0695 \pm 0.0649$ | $-3.8286 \pm 2.0938$ | $0.6497 \pm 0.0016$ |
|        | F814W           | exp                                                  | $-0.0909 \pm 0.0438$ | $-3.2279 \pm 1.0425$ | $0.6086 \pm 0.0016$ |
| WFC3   | F336W           | pow                                                  | $-0.0064 \pm 0.0028$ | $-1.8004 \pm 0.4633$ | $1.6472 \pm 0.0022$ |
|        | F390W           | exp                                                  | $-0.0763 \pm 0.0061$ | $-0.7961 \pm 0.1602$ | $1.486 \pm 0.0035$  |
|        | F438W           | exp                                                  | $-0.0839 \pm 0.0284$ | $-2.5967 \pm 0.6941$ | $1.3507 \pm 0.0017$ |
|        | F475W           | pow                                                  | $-0.0224 \pm 0.0041$ | $-1.3107 \pm 0.1793$ | $1.2233 \pm 0.0031$ |
|        | F555W           | exp                                                  | $-0.2282 \pm 0.0396$ | $-3.0752 \pm 0.3704$ | $1.0776 \pm 0.0017$ |
|        | F606W           | exp                                                  | $-0.2271 \pm 0.0368$ | $-2.9707 \pm 0.3438$ | $0.9622 \pm 0.0017$ |
|        | F625W           | pow                                                  | $-0.0048 \pm 0.0028$ | $-1.8035 \pm 0.6184$ | $0.879 \pm 0.0022$  |
|        | F775W           | exp                                                  | $-0.0713 \pm 0.0695$ | $-3.9365 \pm 2.1978$ | $0.6558 \pm 0.0016$ |
|        | F814W           | pow                                                  | $-0.0058 \pm 0.0029$ | $-1.7434 \pm 0.5318$ | $0.6149 \pm 0.0023$ |
| Gaia   | G               | pow                                                  | $-0.0952 \pm 0.0042$ | $-1.2853 \pm 0.043$  | $1.044 \pm 0.0032$  |
|        | G <sub>bp</sub> | pow                                                  | $-0.1258 \pm 0.0081$ | $-0.7984 \pm 0.0499$ | $1.2562 \pm 0.0069$ |
|        | G <sub>rp</sub> | pow                                                  | $-0.013 \pm 0.0031$  | $-1.6863 \pm 0.2444$ | $0.6753 \pm 0.0023$ |

Table 3.1: Coefficient values produced for each filter via  $A_{\text{exp}}$  or  $A_{\text{exp}}$  fitting, as appropriately labelled. Any filters missing from this table are those with data that could not be accurately fitted using either function.

| Filter | Function<br>( $A_{\text{pow}}$ or $A_{\text{exp}}$ ) | Coefficients         |                      |                     |
|--------|------------------------------------------------------|----------------------|----------------------|---------------------|
|        |                                                      | $a$                  | $b$                  | $c$                 |
| F218W  | exp                                                  | $-0.0763 \pm 0.0061$ | $-0.7961 \pm 0.1602$ | $1.486 \pm 0.0035$  |
| F225W  | exp                                                  | $-0.0839 \pm 0.0284$ | $-2.5967 \pm 0.6941$ | $1.3507 \pm 0.0017$ |
| F275W  | pow                                                  | $-0.0224 \pm 0.0041$ | $-1.3107 \pm 0.1793$ | $1.2233 \pm 0.0031$ |
| F300X  | blah****                                             | $-0.2282 \pm 0.0396$ | $-3.0752 \pm 0.3704$ | $1.0776 \pm 0.0017$ |

Table 3.2: Coefficient values for non-trivial functions produced for fitting to UV filter data.

This was done to reflect the fact that, on one hand, the assumption of a constant extinction coefficient is valid in the plateau region and, on the other, given the position of the MSTO in terms of stellar model  $T_{\text{eff}}$  values, it would be more prudent to ensure that the upper main sequences resulting from both approaches to extinction coincide in the CMD, making it easier to see any disagreements in the turn-off ages. For each of these plots,  $A_V$  was fixed at a value of 1.0.

### 3.2.1 ACS

The CMD chosen for the ACS was the F435W-(F435W-F814W) axis combination. This CMD is useful as it pairs the bluest and reddest wide-field filters for the ACS in its colour index, which is the index most likely to distinguish between objects with a large range of effective temperatures, making it useful for modelling the main sequence and MSTO, the two most important CMD components for calculating cluster isochrone ages.

### 3.2.2 WFC3

The CMD chosen for the ACS was the F435W-(F435W-F814W) axis combination. This CMD is useful as it pairs the bluest and reddest wide-field filters for the ACS, which produces larger spectral colours.\*\*\*\*

### 3.2.3 Gaia

The photometric filters in Gaia, as shown by their respective response functions in Figure 2.2, are designed such that the only reasonable colour index is the  $(G_{\text{bp}} - G_{\text{rp}})$  index. The  $G$  filter, being the widest filter of the three available wide-field filters. This CMD is useful as it pairs the bluest and reddest wide-field filters for the ACS, which produces larger spectral colours.\*\*\*\*

## 3.3 NGC 6793

\*\*\*\*The errors in the parallax data for objects assigned to NGC 6793 were significant, particularly for stars in the lower main-sequence - understandably, since they are the faintest objects in the data and therefore are more difficult to track against the background light sources. This leads to errors in the predicted  $M_{\text{ext},X}$  magnitudes, which is calculated by rearranging Equation 1.4. The significance of the parallax errors in the main sequence is such that, any differences between isochrones with similar parameters are rendered insignificant. This is the case irrespective of photometric errors in the observed fluxes from the photometric filters.

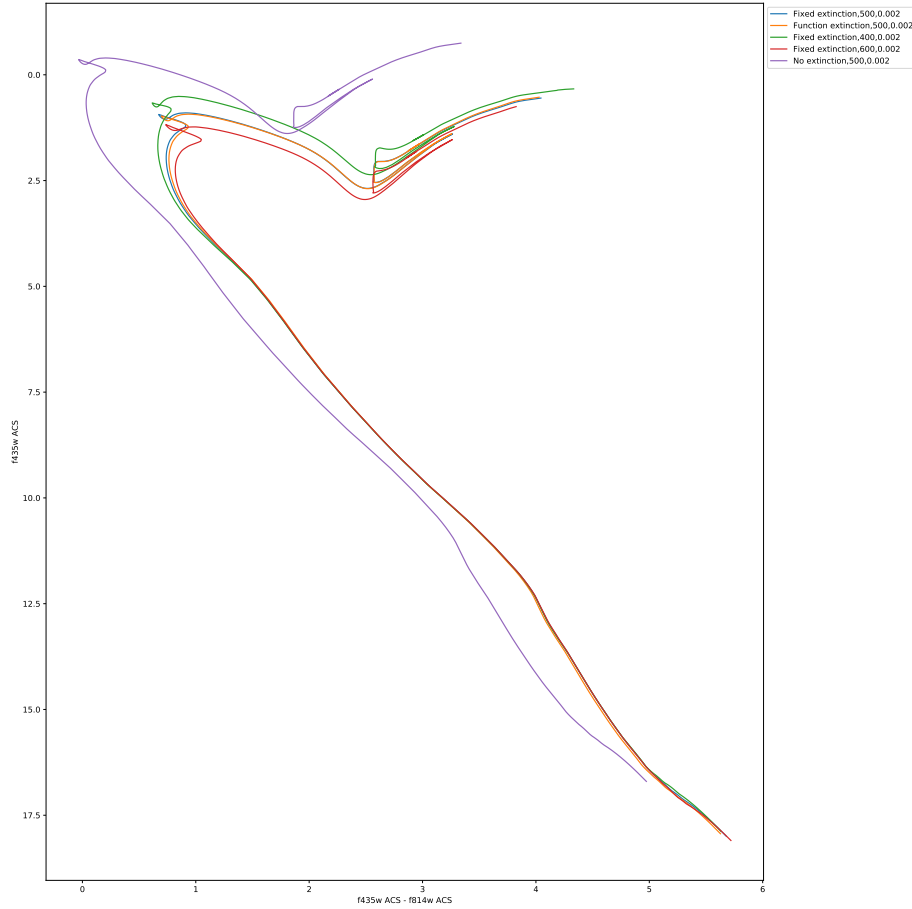


Figure 3.1: ACS F435W-(F435W-F814W) CMD with a fixed extinction coefficient equal to  $(A_X/A_V)_{MS}$  for each filter

Since the table for photometric fluxes did not include photometric errors, the parallax errors alone accounted for the total error in the calculated  $M_{\text{ext},X}$ . Therefore, the errors on the flux measurements were exactly equal in all filters for a given star. The errors on the  $(G_{\text{bp}} - G_{\text{rp}})$  color index were calculated as standard, by adding the individual filter errors in quadrature, giving the color errors which were a factor of  $\sqrt{2}$  greater than those for the individual filter fluxes.

There are highly significant errors for the individual objects in the Gaia data propagation, even when assuming the only source of error is from parallax measurements, as shown in Figure 3.9. The magnitude of the errorbars dwarf any changes in isochrones due to extinction coefficient treatments in the main sequence. For the few objects in the data with

\*\*\*\*Get zoom in on turn-off region

All the isochrones, as shown in Section\*\*\*\*, are sensitive both to the reference

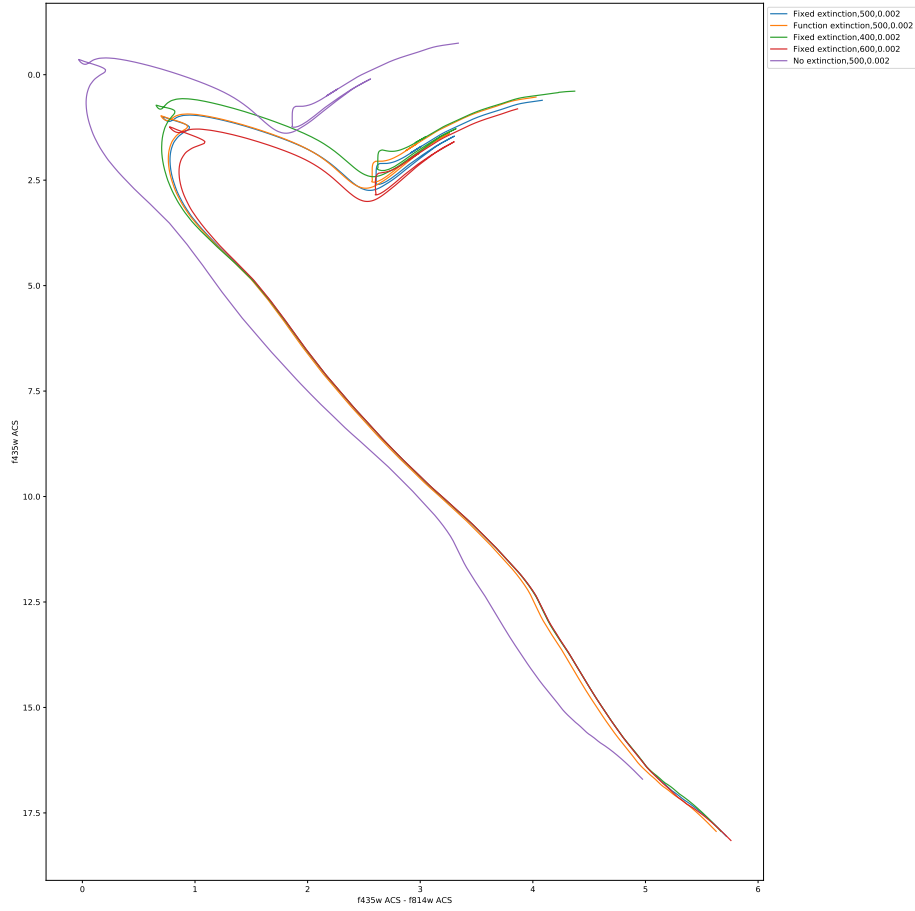


Figure 3.2: ACS F435W-(F435W-F814W) CMD with a fixed extinction coefficient equal to  $(A_X/A_V)_{\text{plat}}$  for each filter

extinction coefficient value  $A_V$  and to the value of  $A_X/A_V$  for the fixed-coefficient case, which is to be expected. Some individual parts of the isochrones relevant to this study are additionally sensitive to other isochrone parameters:

1. The position of the MSTO is sensitive to the treatment of  $A_X/A_V$ , as shown in Section\*\*\*\*, and the isochrone age.
2. The position of the lower main sequence is significantly more sensitive to metallicity than other parts of the isochrone.

\*\*\*\*compare BaSTI and PARSEC isochrone softwares using Gontcharov et al. (2019) figures

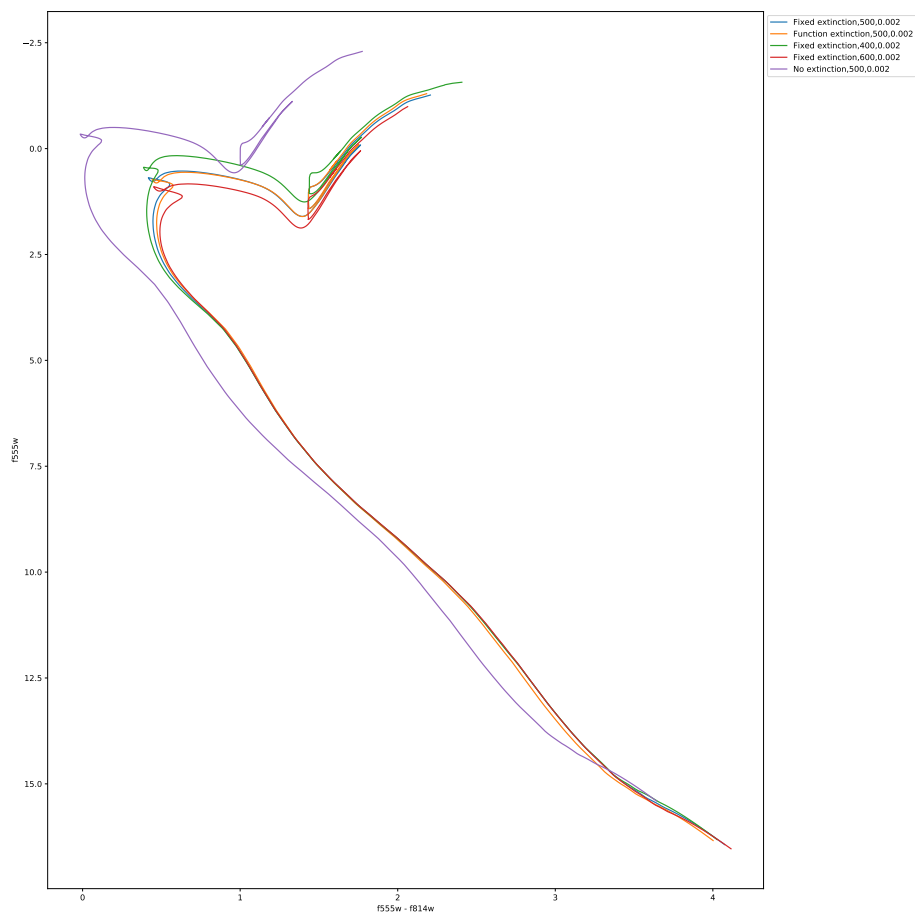


Figure 3.3: WFC3 F555W-(F555W-F814W) CMD with a fixed extinction coefficient equal to  $(A_X/A_V)_{MS}$  for each filter



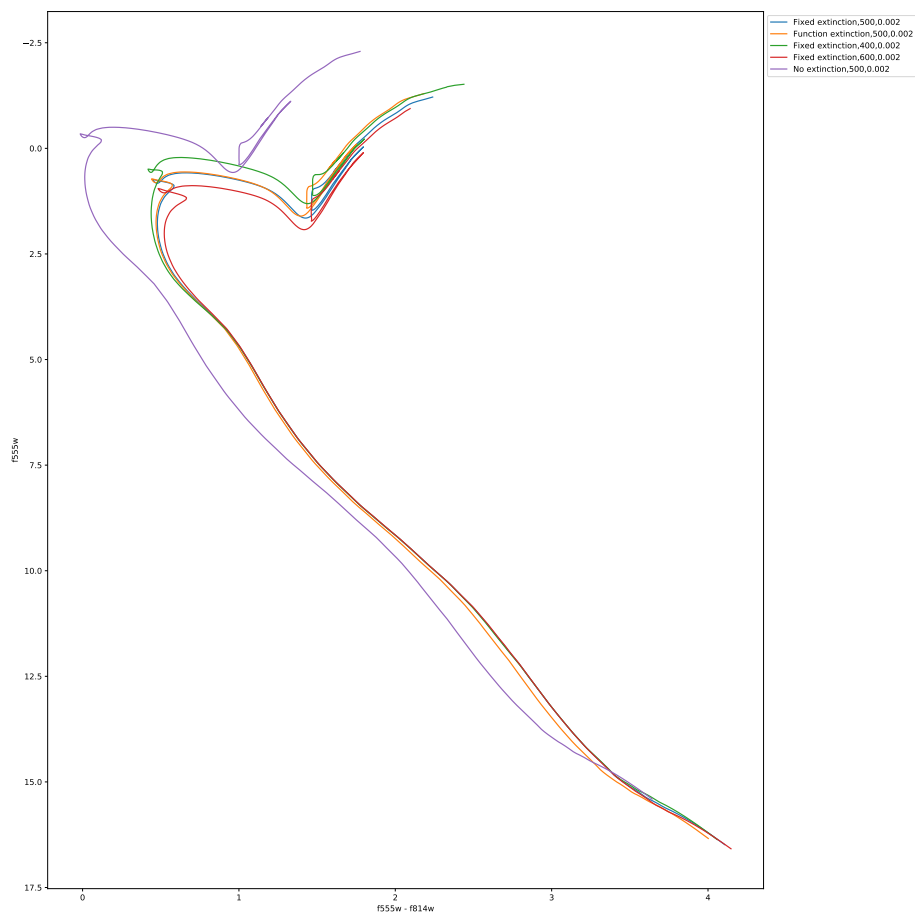


Figure 3.4: WFC3 F555W-(F555W-F814W) CMD with a fixed extinction coefficient equal to  $(A_X/A_V)_{plat}$  for each filter

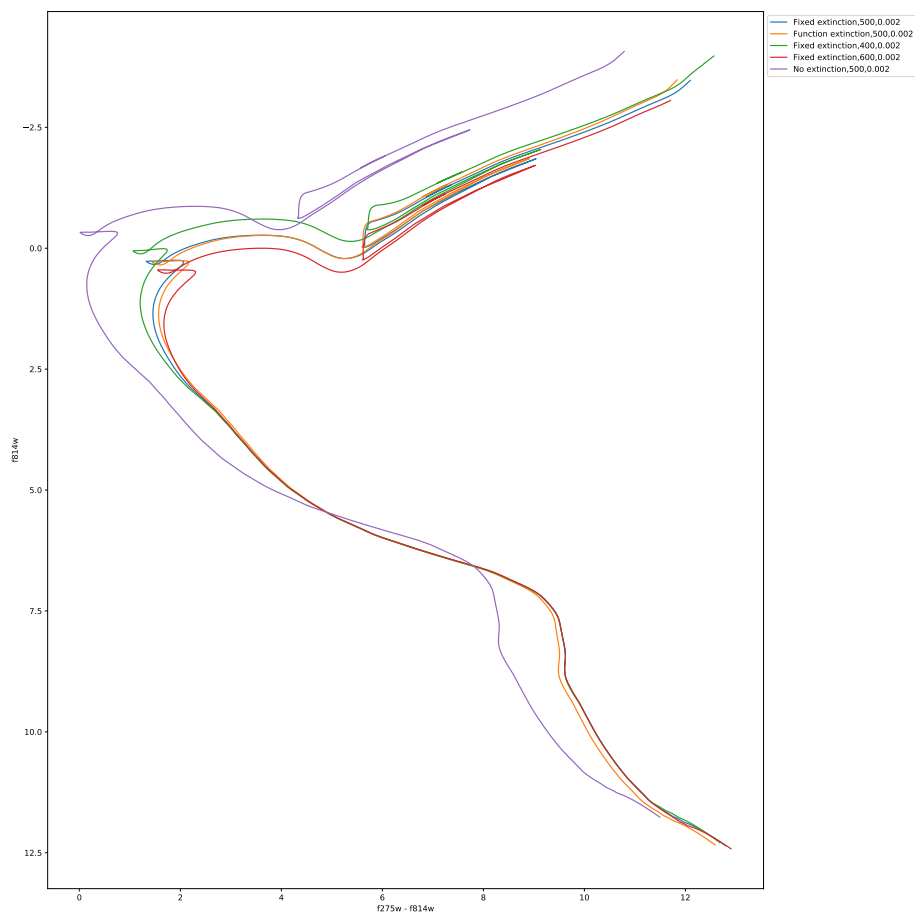


Figure 3.5: WFC3 F814W-(F275W-F814W) CMD with a fixed extinction coefficient equal to  $(A_X/A_V)_{MS}$  for each filter

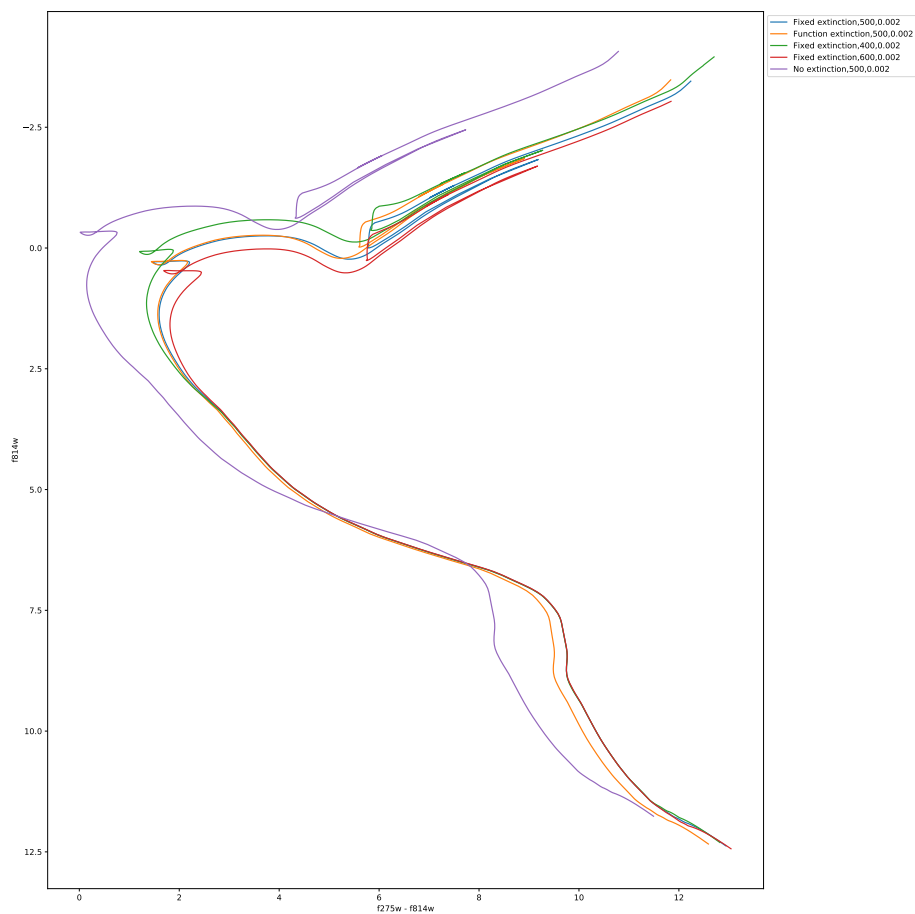


Figure 3.6: WFC3 F814W-(F275W-F814W) CMD with a fixed extinction coefficient equal to  $(A_X/A_V)_{plat}$  for each filter

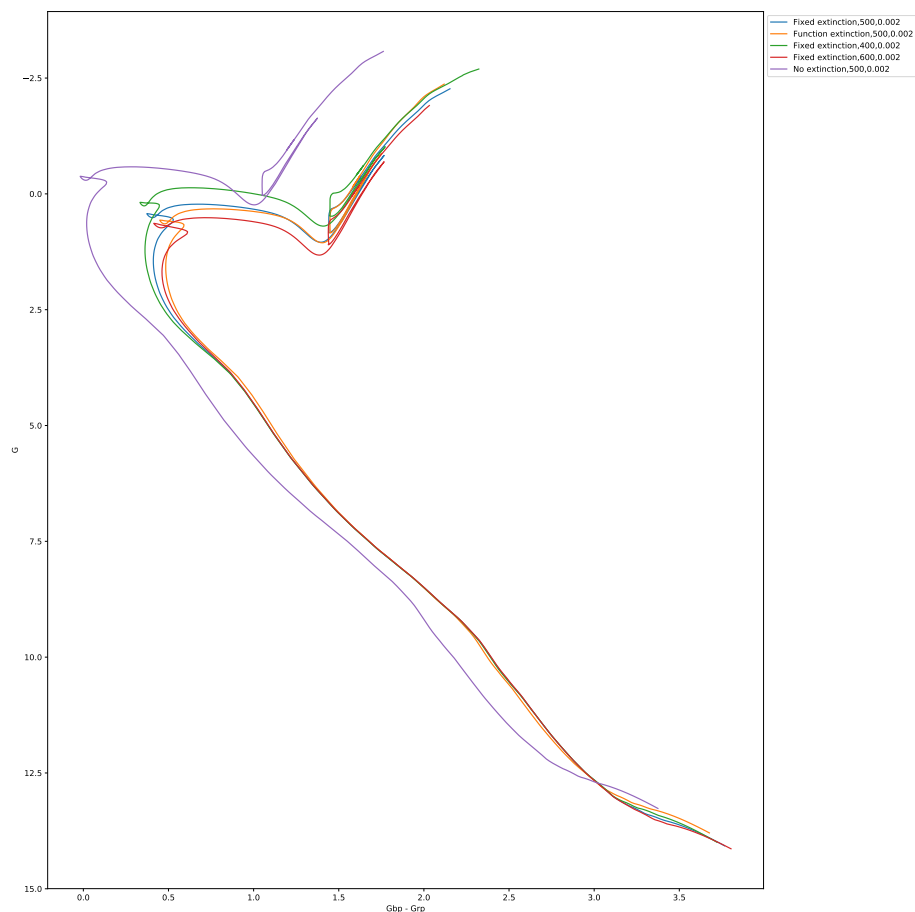


Figure 3.7: Gaia  $G$ -( $G_{bp}$ - $G_{rp}$ ) CMD with a fixed extinction coefficient equal to  $(A_X/A_V)_{MS}$  for each filter

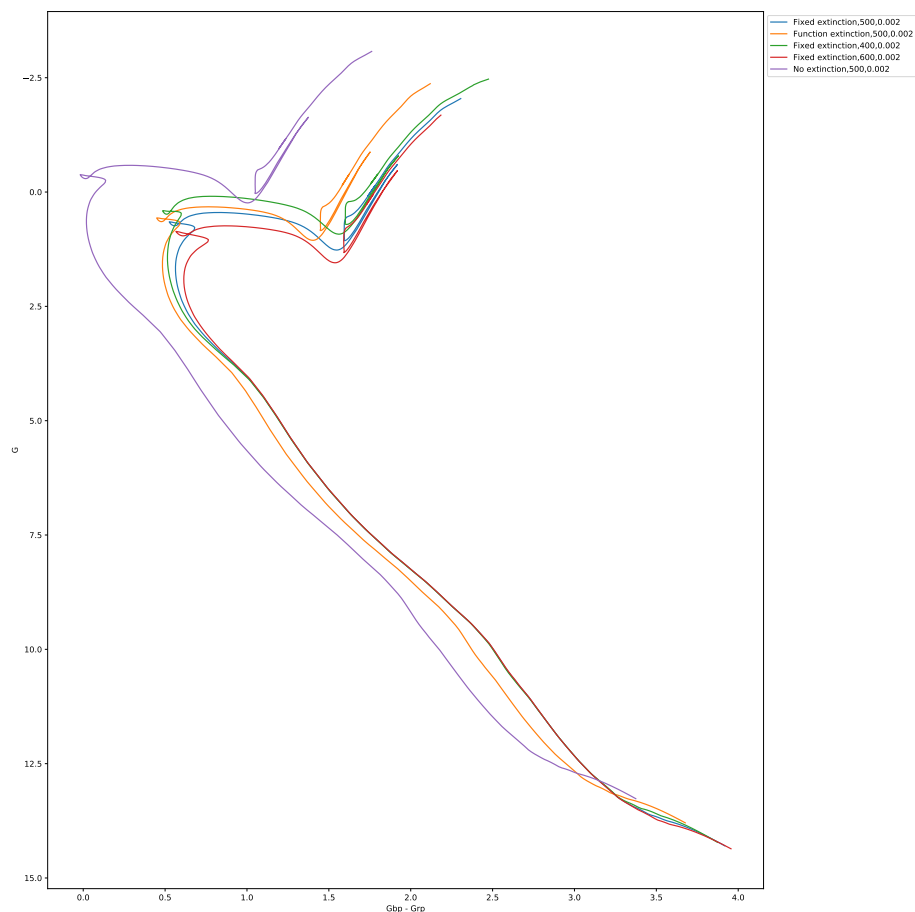


Figure 3.8: Gaia  $G$ -( $G_{bp}$ - $G_{rp}$ ) CMD with a fixed extinction coefficient equal to  $(A_X/A_V)_{plat}$  for each filter

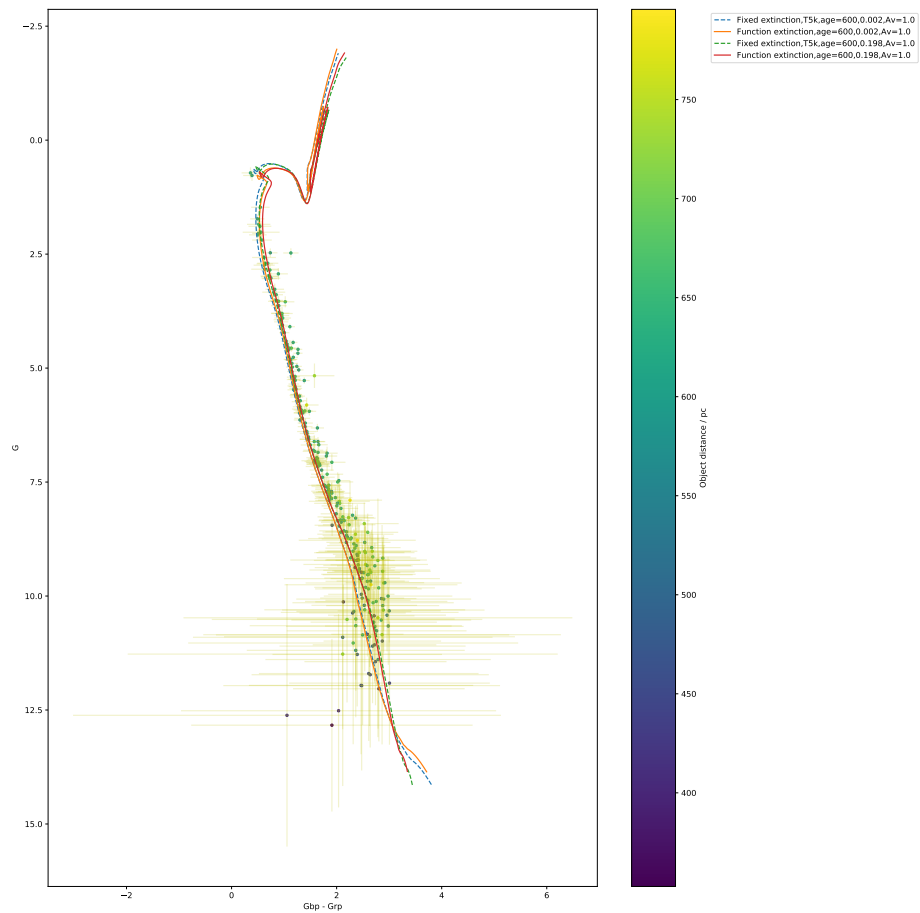


Figure 3.9: Gaia CMD of NGC 6793 with errorbars included.

## Chapter 4

### Conclusion & future work

In all cases, applying a fixed extinction to all points in an isochrone causes the main-sequence turn-off to occur at a more luminous, bluer point in a given CMD than the MSTO point for an extinction coefficient described using a function fitted to empirically derived data.

# Bibliography

- Bessell M. S., 1990, *PASP*, 102, 1181
- Cardelli J. A., Clayton G. C., Mathis J. S., 1989, *ApJ*, 345, 245
- Casagrande L., VandenBerg D. A., 2014, *MNRAS*, 444, 392
- Casagrande L., VandenBerg D. A., 2018, *MNRAS*, 479, L102
- Castellani V., Chieffi A., Straniero O., 1992, *ApJS*, 78, 517
- Castelli F., Kurucz R. L., 2004, *ArXiv Astrophysics e-prints*
- Fitzpatrick E. L., 1999, *PASP*, 111, 63
- Gaia Collaboration et al., 2018, *A&A*, 616, A10
- Girardi L., Bertelli G., Bressan A., Chiosi C., Groenewegen M. A. T., Marigo P., Salasnich B., Weiss A., 2002, *A&A*, 391, 195
- Girardi L., et al., 2008, *PASP*, 120, 583
- Gontcharov G. A., Mosenkov A. V., Khovritchev M. Y., 2019, *MNRAS*, 483, 4949
- Gustafsson B., Edvardsson B., Eriksson K., Jørgensen U. G., Nordlund Å., Plez B., 2008, *A&A*, 486, 951
- Hidalgo S. L., et al., 2018, *ApJ*, 856, 125
- Johnson H. L., Morgan W. W., 1953, *ApJ*, 117, 313
- Jordi C., et al., 2010, *A&A*, 523, A48
- Kalirai J. S., Baggett S., Borders T., Rajan A., 2010, Technical report, The Photometric Performance of WFC3/UVIS: Temporal Stability Through Year 1
- Kharchenko N. V., Piskunov A. E., Röser S., Schilbach E., Scholz R.-D., 2005, *A&A*, 438, 1163



- Kurucz R., 1993, ATLAS9 Stellar Atmosphere Programs and 2 km/s grid. Kurucz CD-ROM No. 13. Cambridge, Mass.: Smithsonian Astrophysical Observatory, 1993., 13
- MacKenty J. W., Kimble R. A., O'Connell R. W., Townsend J. A., 2010, in Space Telescopes and Instrumentation 2010: Optical, Infrared, and Millimeter Wave. p. 77310Z
- O'Donnell J. E., 1994, ApJ, 422, 158
- Paczyński B., Stanek K. Z., 1998, ApJ, 494, L219
- Pietrinferni A., Cassisi S., Salaris M., Castelli F., 2004, ApJ, 612, 168
- Rieke G. H., Lebofsky M. J., 1985, ApJ, 288, 618
- Sarajedini A., et al., 2007, ApJ, 133, 1658
- Schilbach E., Kharchenko N. V., Piskunov A. E., Röser S., Scholz R.-D., 2006, A&A, 456, 523
- Valencic L. A., Clayton G. C., Gordon K. D., 2004, ApJ, 616, 912